Surface Acoustic Wave Cavity Optomechanics with Atomically Thin *h*-BN and WSe₂ Single-Photon Emitters

Sahil D. Patel,[†] Kamyar Parto,[†] Michael Choquer,[†] Nicholas Lewis, Sammy Umezawa,
Landon Hellman, Daniella Polishchuk, and Galan Moody[*]

Electrical and Computer Engineering Department, University of California, Santa Barbara, California 93106,
USA

Surface acoustic waves (SAWs) are a versatile tool for coherently interfacing with a variety of solid-state quantum systems spanning microwave to optical frequencies, including superconducting qubits, spins, and quantum emitters. Here, we demonstrate SAW cavity optomechanics with quantum emitters in two-dimensional (2D) materials, specifically monolayer WSe₂ and *h*-BN, on a planar lithium niobate SAW resonator driven by superconducting electronics. Using steady-state photoluminescence spectroscopy and time-resolved single-photon counting, we map the temporal dynamics of modulated 2D emitters under coupling to different SAW cavity modes, showing energy-level splitting consistent with deformation potential coupling of 35 meV/% for WSe₂ and 12.5 meV/% for *h*-BN visible-light emitters. We leverage the large anisotropic strain from the SAW to modulate the excitonic fine-structure splitting in WSe₂ on a nanosecond timescale, which may find applications for on-demand entangled-photon-pair generation from 2D materials. Cavity optomechanics with SAWs and 2D quantum emitters provide opportunities for compact sensors and quantum electro-optomechanics in a multifunctional integrated platform that combines phononic, optical, and superconducting electronic quantum systems.

I. INTRODUCTION

Coupling of solid-state artificial atoms, such as optically active defects and color centers, with confined acoustic modes in optomechanical resonators is an elegant approach for coherently controlling, transferring, and entangling a variety of quantum degrees of freedom, including photons, phonons, and spins [1,2]. In solids, microwave phonons and optical photons have similar wavelengths and can be confined into small mode volume cavities that enable efficient mode overlap and strong interactions. Many platforms have been developed to mediate these interactions [3], including mechanical membranes [4,5], hybrid photonic-phononic crystals [6–8], and surface acoustic wave (SAW) resonators [9–11]. Single-photon emitters (SPEs) embedded within optomechanical cavities are remarkably sensitive to local strain, exhibiting frequency shifts nearly 2 orders-of-magnitude larger (about 10 GHz/pm) than microscale optical resonators (about

100 MHz/pm) [12]. The use of SPEs provides a strong optical nonlinearity that ensures only individual photons are emitted, typically with subnanowatt optical power requirements. When operated in the sideband-resolved regime using gigahertz-frequency resonators, parametric modulation of SPEs enables microwave-frequency information to be encoded as optical photons, which may enable efficient and low-noise transduction between microwave and optical frequency qubits [13].

A variety of SPE optomechanical platforms have been developed for these purposes, including defect centers in diamond [14–16], silicon carbide [17], and semiconductor quantum dots (QDs) [18–22], with a vacuum optomechanical coupling rate g_0 as high as about 1 MHz recently demonstrated with SAW resonators [12]. The recent discovery of SPEs in two-dimensional (2D) materials [23,24], such as WSe₂ [25–29] and hexagonal boron nitride [30,31], provides an opportunity to further enhance the coupling while simplifying the device and fabrication complexity. Two-dimensional SPEs, which originate from crystalline defects in the host material, exhibit high optical extraction efficiency and brightness with detection rates up to 25 MHz [32–34], indistinguishable [35] and near transform-limited linewidths [36], high single-photon purity, unique spin-valley phenomena [37–39], high working temperatures [30,40,41], and site selective engineering [42–45]. The layered structure of 2D

---

[*]moody@ucsb.edu
[†]These authors contributed equally to this work.

materials arising from van der Waals forces ensures that the defects are two dimensional and are able to function at surfaces, devoid from any surface states, allowing for strong proximity interaction with their surrounding environment.

This strong proximity interaction, in addition to the site-specific fabrication and relaxed lattice-matching requirements, makes 2D SPEs an ideal two-level system to be integrated with optomechanical resonators. Proximity effects allow for efficient deformation potential coupling, as illustrated in Figs. 1(a) and 1(b), while the ability to deterministically transfer 2D monolayers onto nearly any surface allows for nanoscale precision in positioning of a single SPE within optomechanical resonators [45]. Indeed, modulation of few-layer h-BN SPEs with propagating SAWs has resulted in large deformation potential coupling [46]; however, to date, integration of 2D SPEs with high-quality SAW resonators, a critical step for exploring the potential of 2D materials for quantum optomechanics, has not yet been explored.

In this work, we parametrically modulate the resonance frequency of SPEs in monolayer WSe$_2$ and multilayer h-BN integrated with a LiNbO$_3$ SAW resonator driven by superconducting electronics and study the coupling mechanisms, strain susceptibility, and potential for acoustic quantum-regime operation. We demonstrate cavity phonon-SPE coupling with deformation potential coupling of at least 35 meV/% for WSe$_2$ and 12.5 meV/% for h-BN, which is larger than or comparable to alternative SPE host materials [13]. The dynamics of the SPE-SAW cavity system are measured through time-resolved, stroboscopic, and steady-state photoluminescence spectroscopy. Notably, in WSe$_2$, by sweeping the SAW frequency and the cavity phonon occupation, we demonstrate exquisite control over the local strain. We show that, when driven on resonance, the SAW modulates and mixes the emission from exciton fine-structure transitions that have been attributed to anisotropic exchange [26] and intervalley symmetry breaking in the presence of defects [47], providing a dynamical on-chip control knob for mixing of the WSe$_2$ SPE doublets. These results establish a new experimental platform that combines cavity optomechanics with 2D material quantum optics, paving the way for efficient and high-speed manipulation of 2D quantum emitters for single-photon switching, tuning and stabilization, and entangled-photon-pair generation.

II. SAW-EMITTER DEVICE FABRICATION AND CHARACTERIZATION

SAW cavities were fabricated on bulk LiNbO$_3$ using a combination of NbN sputtering and electron-beam lithography to define superconducting Bragg reflectors and interdigital transducers (IDTs). The periodicity of the mirrors and the acoustic impedance within the mirrors define the

mirror acoustic stopband and the spectral reflection window, which is centered near 300 or 400 MHz for a variety of lengths spanning 900 to 2600 μm. Electromechanical measurements of the S_{11} parameter for the cavity yield internal quality factors of the order of 12 000 and external quality factors of 7000, which are limited by the loss due to the mirrors (see Appendix A). Using an all dry-transfer technique, monolayer WSe$_2$ and plasma annealed h-BN flakes [24] were exfoliated and transferred to the SAW cavities (see Appendix B for the fabrication procedure) [48]. Cavity reflectivity (S_{11}) measurements taken at 4.4 K confirm the presence of the cavity modes. A simultaneous fit to the magnitude and phase (see Appendix A) demonstrates that the cavity is in the undercoupled regime with an average intrinsic quality factor of 1900 and an extrinsic quality factor of 3700 after the flake transfer, which are similar to loaded quality factors of SAWs integrated with III-V QDs [20].

III. CAVITY OPTOMECHANICS WITH WSe$_2$ AND h-BN SPES

WSe$_2$ and h-BN SPEs are identified using steady-state photoluminescence (PL) spectroscopy. SPEs in WSe$_2$ and h-BN appear as spatially localized and spectrally sharp peaks in the PL spectra, as illustrated by the narrow filled peaks in Figs. 1(c) and 1(e). The lineshapes are instrument-response limited with a resolution of about 200 μeV. Emission of single photons is verified by the antibunching dip at zero time delay in the second-order autocorrelation function shown in Figs. 1(d) and 1(f) for WSe$_2$ and h-BN, respectively (see Appendix C for details of the experimental setup). While we have identified many emitters in WSe$_2$ and h-BN that couple to the SAWs, in this paper we present a set of comprehensive measurements on the same emitter for each respective material.

After identifying the SPE and SAW cavity resonances, the SAW drive frequency applied to the IDT for each device was fixed at the location of each cavity resonance, and the PL measurement was repeated. When driving the SAW on resonance, a standing surface acoustic wave is formed inside of the cavity. Depending on the position of the SPE relative to the node and antinode of the standing wave, the SPE experiences dynamic compressive and tensile strain from the SAW [Fig. 1(a)]. Through deformation potential coupling, the strain modulates the local band gap of the material, resulting in a temporally varying energy shift of the SPE at the frequency of the SAW mode. Within the Franck-Condon framework, as illustrated in Fig. 1(b), both the ground state and the excited state of the emitters interact with the phonon vibrational modes with an intensity determined by the Huang-Rhys factor. A surface acoustic wave cavity mode can be treated similar to a bulk phonon in this description. On resonance, the cavity mode interacts strongly with the ground and excited
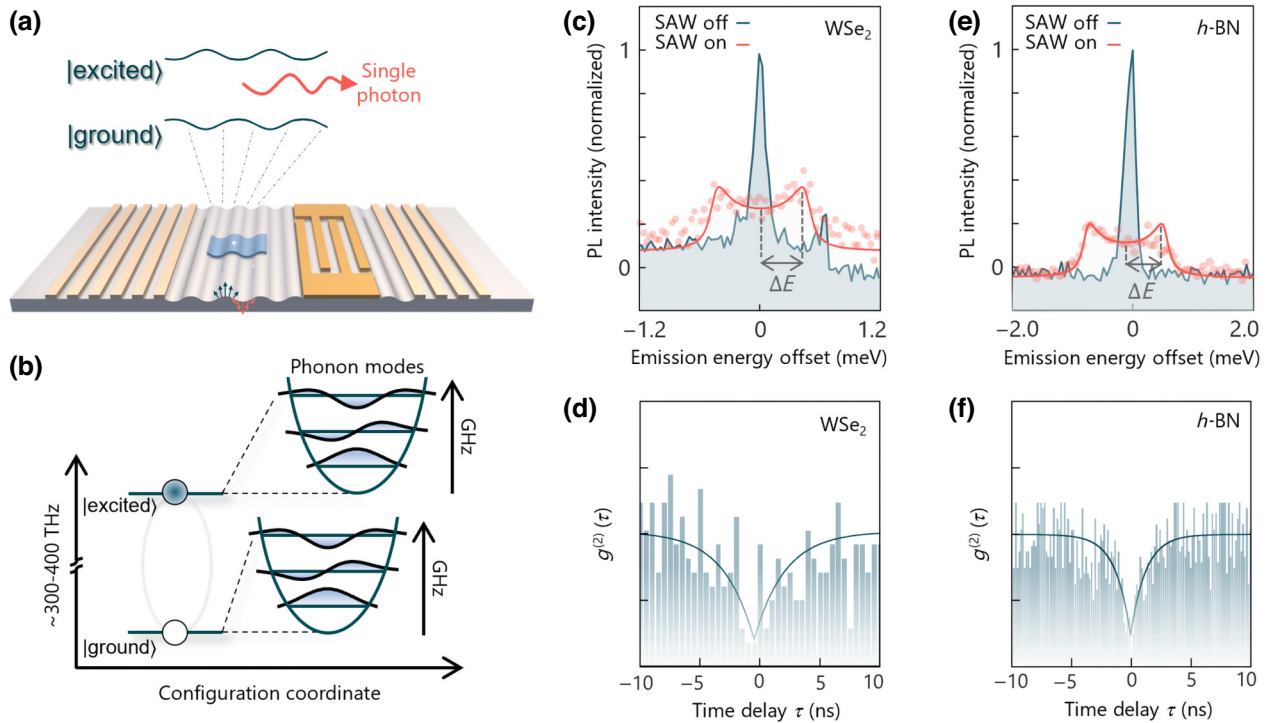
FIG. 1.   LiNbO$_3$ SAW integration with 2D-based single-photon emitters. (a) Schematic illustration of a 2D material hosting a single-photon emitter modulated in a surface acoustic wave cavity. The sketch denotes the modulation of the ground and excited states of the emitter over time. The out-of-plane strain vector is indicated by the arrows on the surface of the substrate. (b) Franck-Condon representation of the interaction between cavity phonons and the emitter. Both ground and excited states are coupled to phonon modes with energies significantly lower than the optical transition energy. (c) Representative photoluminescence (PL) spectra of SPEs in the WSe$_2$ monolayer measured at 4.4 K when driven on resonance (303.6 MHz) and off resonance (301.5 MHz) with a SAW cavity mode (see Fig. 2). (d) The second-order autocorrelation function of a WSe$_2$ emitter demonstrating photon antibunching. (e) Representative PL spectra of an SPE in h-BN measured at 4.4 K when driven on resonance (398 MHz) and off resonance (397.5 MHz) with a SAW cavity mode. (f) The second-order autocorrelation function demonstrating photon antibunching for a thermally activated h-BN SPE.

states of the emitter and imprints its signature on the photoluminescence spectrum. In the sideband-resolved regime where the frequency of the resonant cavity phonon is larger than the linewidth of the emitter (typically in the gigahertz range), the PL spectra consist of a series of replicas of the zero-phonon line (ZPL) spaced by the frequency of the resonance cavity phonon mode. In the case where the linewidth of the emitter is larger than the cavity phonon frequency (as in the present study), the slow modulation timescale compared to the emission merges the phonon replicas, which appear as a double-peak structure.

Figures 1(c) and 1(e) show representative modulated spectra from a WSe$_2$ and h-BN emitters when the SAW cavity is driven on resonance (shown for different drive powers due to differences in the deformation potential coupling efficiency, as described below). The narrow Lorentzian lineshape of the SPEs is split into a double-peak structure with a peak-to-peak separation of $2\Delta E =$ 0.92 meV for WSe$_2$ and $2\Delta E = 1.75$ meV for h-BN. This double-peak structure is a clear signature of SPE-SAW coupling, consistent with previous observations from III-V

QDs [1] and SiC vacancy centers [17] coupled to surface acoustic wave cavities. The PL signals were fit to a Lorentzian function modulated by a sinusoidal interaction in the time domain to extract the modulation energy ΔE [49]. This process is further described in Appendix D.

Next, the evolution of the PL spectrum as a function of the SAW cavity frequency at a constant power (4 dBm for WSe$_2$ and 11 dBm for h-BN) was measured. The maximum modulation of the PL lineshape occurs at the SAW cavity resonant frequencies for both h-BN and WSe$_2$. In WSe$_2$, as seen in Figs. 2(a) and 2(b), the three resonances at 299.4, 301.0, and 303.6 MHz are associated with clear splitting, distinctly different from when driving the SAW cavity off-resonance. Interestingly, this emitter shows a nonzero splitting between 299.0–301.5 MHz, which may be attributed to mode mixing between the neighboring cavity resonances due to the SPE being spatially located somewhere between a node and antinode for this frequency range, as similarly reported for QDs [20]. The nonzero splitting may also be due to nonlinear effects such as acoustic wave mixing [50]. The characteristic spectral

jitter in Fig. 2(a) arises from charge noise due to nonresonant excitation [23]. The spectral diffusion exhibited by the WSe_2 emitters contributes to inhomogeneous broadening of the linewidth, as observed previously [51–53]. Multiple timescales contribute to spectral diffusion. A submillisecond component—faster than the PL spectrum integration time—broadens the zero-phonon linewidth, leading to the typically reported WSe_2 linewidths of 100–200 µeV. In addition, a slower timescale component (tens of seconds to minutes) of spectral diffusion results in a time-varying zero-phonon line resonance frequency. Indeed, this is what is observed as the discrete jumps in the spectrum in Fig. 2(a), most evident near 301.5 MHz additional data of a different WSe_2 emitter showing similar spectral diffusion is shown in Figs. 11(a) and 11(b)). Among the WSe_2 emitters that were measured, only those that exhibited linewidths below 1 meV without applied SAW modulation exhibited a measurable splitting. Among these emitters, nearly 75% exhibited coupling to at least one of the cavity modes [Fig. 2(b)], a result that is not surprising given that the positions of the SPEs with respect to the node or antinode of the cavity are randomly distributed in these devices. The spectra in Fig. 2(a) also display a gradual broadening of the peak from 302 to 303.5 MHz due to nonlinear and acoustic wave-mixing phenomena (similar to the broadening in the 299–301 MHz range). Notably, the SPE in Fig. 2(a) consists of a doublet with a fine-structure splitting (FSS) of the order of 700 µeV, which has previously been attributed to anisotropic strain [26] and intervalley excitonic mixing in WSe_2 [41,47,54]. Interestingly, both peaks of the doublet exhibit the same splitting as a function of frequency, and given the extent of the modulation, the two peaks can overlap and mix at the position of the cavity resonances. This mixing has implications for

photon-state engineering and entanglement, as discussed below.

The trend is similar in *h*-BN, as seen in the modulated spectral map in Fig. 2(c). Clear splitting is observed for the cavity resonance at 398.0 MHz, whereas only spectral broadening is observed for the cavity mode at 397.2 MHz. The emitter linewidth remains instrument-response limited when the cavity is driven off resonance. Notably, these *h*-BN emitters exhibit less jitter compared to WSe_2. Among the *h*-BN emitters identified in our devices, only 10% of them exhibit SAW-induced splitting, which is a considerably lower yield than WSe_2; however, given that the *h*-BN flakes are multilayer, we expect that the coupling strength of the SAW to the emitter would be proportional to the proximity of the defect to the surface of the lithium niobate. This is especially the case in vdW materials where the in-plane compressive or tensile stress transfers weakly in the *c*-axis direction due to weak out-of-plane interactions, as evidenced by the extremely low *c*-axis thermal conductivity of 2D materials [55].

IV. STROBOSCOPIC MEASUREMENTS AND DEFORMATION POTENTIAL COUPLING

While it is clear that the SPEs are modulated by the SAWs, to rule out alternative explanations, such as induced nonradiative decay or local heating, we perform time-resolved and stroboscopic PL measurements to map out the SAW dynamics. We focus on WSe_2 SPE devices, but similar arguments apply to *h*-BN SPE devices as well. First, Fig. 3(a) shows the time-resolved PL dynamics of the WSe_2 emitter from Fig. 1 with ($P_{rf} = 6$ dBm) and without power applied to the SAW IDT. In both cases, the SPE recombination lifetime is longer than about 2 ns,
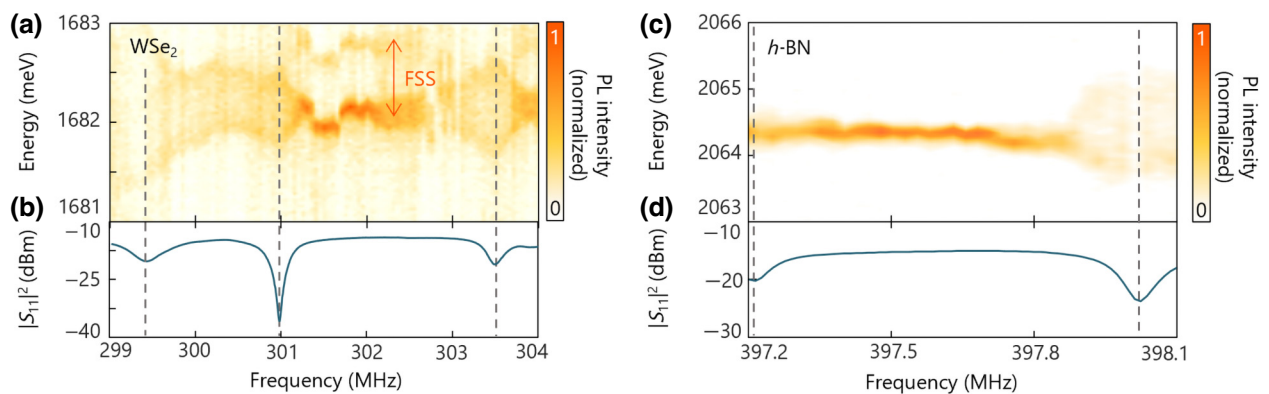

FIG. 2.   Microwave frequency-dependent energy splitting of a WSe_2 and *h*-BN single-photon emitter obtained from 4.4-K PL modulation spectroscopy. (a) Representative WSe_2 emitter resonance modulation as a function of applied frequency to the SAW cavity. Cavity resonances are denoted by vertical dashed lines. The spectral jumps are due to spectral jitter that appear at slow measurement timescales often observed under nonresonant excitation of WSe_2 emitters. A fine-structure-split peak of the zero-phonon line appears 0.8 meV higher in energy than the main signal and is denoted by an arrow. (b) SAW cavity reflection spectrum for the WSe_2 device. (c) The *h*-BN single-photon emission modulation as a function of applied frequency to the SAW cavity. In general, *h*-BN emitters demonstrate higher spectral stability compared to WSe_2. (d) SAW cavity reflection spectrum for the *h*-BN device.
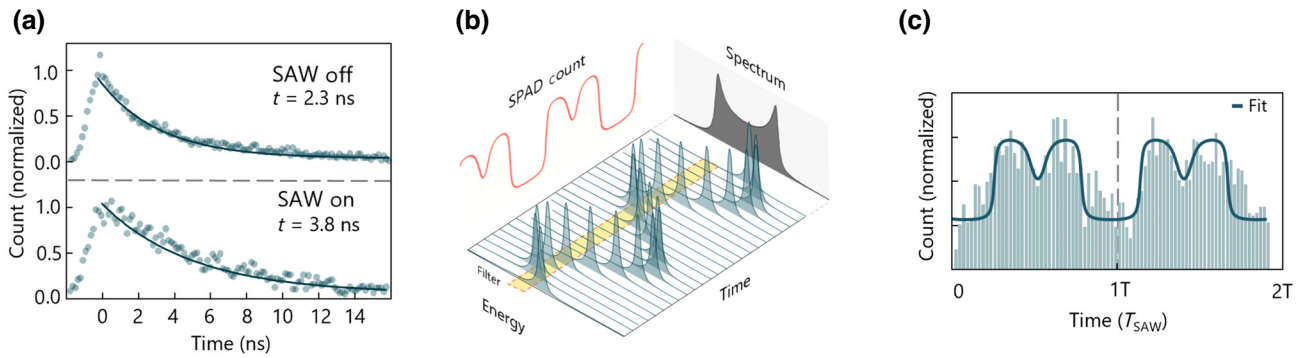
FIG. 3. Time-resolved and stroboscopic photoluminescence measurements. (a) Time-resolved photoluminescence of a WSe$_2$ emitter with the SAW off (top panel) and SAW on (bottom panel). A recombination lifetime > 2 ns is observed in both cases, ruling out any nonradiative, electrodynamic charging, or thermal dissipation mechanisms for the observed modulated signals. (b) Conceptual illustration of the stroboscopic measurement. A monochromator is used to filter out a portion of the modulated signal. The filtered photons are sent to a single-photon avalanche diode (SPAD) and their arrival with respect to the SAW drive signal, which modulates the SPE frequency, is recorded. This allows unravelling of the temporal dynamics of the SPE modulation at nanosecond timescales (dark green peaks), which is otherwise inaccessible due to the slow timescale of steady-state PL measurement (dark gray time-averaged spectrum, which is a projection along the time axis). (c) Results from the stroboscopic measurement (points) with a fit from a Monte Carlo simulation (solid line). Based on the center of the bandpass optical filter, both f_{rf} and $2f_{rf}$ components are observed, as expected.

ruling out any new nonradiative recombination or thermal processes that could lead to faster recombination and broadening of the linewidth in the steady-state PL spectrum. We next performed stroboscopic measurements in which the arrival time of the emitted photons with respect to the phase of the applied SAW waveform is measured through single-photon counting and binning. The emission was spectrally filtered using a monochromator to isolate photons near the wings of the modulated steady-state PL spectrum [Fig. 3(b)]. Results from this measurement are shown by the histogram in Fig. 3(c), which demonstrates clear modulation of the emission waveform at the fundamental SAW frequency of f_{rf}. We observe an additional frequency component at $2f_{rf}$ due to the limited resolution of our monochromator with respect to the total linewidth of our modulated emitter. A fit of the data using a Monte-Carlo-like simulation of a modulated emitter overlapped with a nonideal bandpass filter is shown as the solid line in Fig. 3(c) (see Appendix E for details).

We next performed experiments measuring ΔE as a function of the applied power to the IDT for both WSe$_2$ and h-BN emitters. A plot of the observed energy splitting, $2\Delta E$, as a function of the square root of the applied IDT power (P_{rf}) is shown in Fig. 4. The splitting $2\Delta E$ for WSe$_2$ and h-BN is extracted at each applied power and fit as discussed in Appendix D for the resonant cavity modes at 300.9 and 398 MHz, respectively. From Fig. 4, it is clear that ΔE increases monotonically with the power. On a double-logarithmic scale, we find that $\Delta E \propto \sqrt{P_{rf}}$ with a slope of 0.841 meV/$\sqrt{mW}$ for WSe$_2$ and 1.199 meV/$\sqrt{mW}$ for h-BN (additional data for the WSe$_2$ emitter at different cavity modes is presented in Fig. 12). This linear splitting behavior is consistent with

deformation potential coupling as the predominant physical mechanism between the SAW and SPE that gives rise to the energy modulation [56]. The linear fit of the power dependence allows us to rule out any additional contributions, such as Stark-induced electric field coupling, as having a negligible effect on the SPE splitting and modulation, since this would scale as $\Delta E \propto P_{rf}$ [56].

To extract the deformation potential coupling efficiency, a finite-element simulation is used to extract the tensile
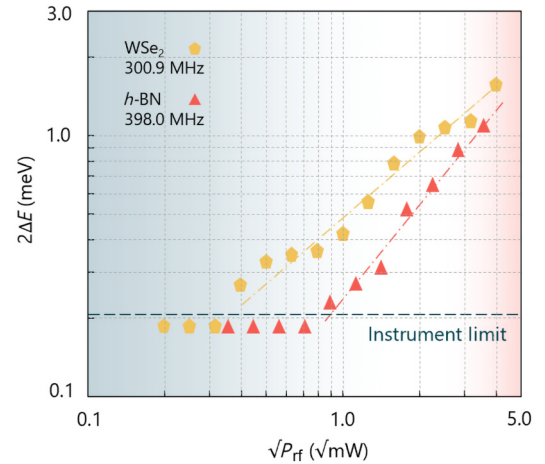

FIG. 4. Power dependence of the emitter lineshape splitting demonstrating deformation potential coupling. Here ΔE is shown as a function of applied power to the SAW IDT. Data for the WSe$_2$ (h-BN) emitter coupled to a 300.9 MHz (398 MHz) SAW cavity resonance are shown in yellow (red). Fits to the power-dependent splitting for the WSe$_2$ and h-BN emitters yield slopes of 0.841 and 1.199 meV/$\sqrt{mW}$, respectively, indicating deformation potential coupling.

strain component along the propagation axis of the cavity at various applied powers to the IDT. A strain of 0.012% at 0-dBm applied power is determined for our 300-MHz resonator with a cavity length $L = 2600$ μm (see Appendix F). Assuming that the strain in the SAW fully transfers to the WSe$_2$ flake, this results in at least an approximate 35 meV/1% frequency shift for WSe$_2$ SPEs; this is a lower bound for the sensitivity of the emitter, given that the van der Waals interaction between the monolayer and LiNbO$_3$ surface could potentially reduce the full transfer of the strain to the SPE. Previously reported measurements of the static energy shift versus strain applied to SPEs lead to an average value of 20-meV/1% (up to 120-meV/1% maximum) for WSe$_2$ emitters. These values are within the same order of magnitude as our extracted coupling efficiency, which suggests that the strain at the LiNbO$_3$ surface is efficiently transferred to the WSe$_2$ monolayer. Similarly for *h*-BN, we measure 0.125 meV splitting at 0 dBm of applied power, leading to 12.5-meV/1% deformation potential coupling for *h*-BN, which is inline with previous estimates from static strain tuning of *h*-BN red single-photon emitters [57].

V. DYNAMIC MODULATION OF SPE EXCITON-BIEXCITON-LIKE FEATURES

After confirming the deformation potential coupling as the microscopic nature of the SPE modulation for both WSe$_2$ and *h*-BN, we turn our attention to a unique feature that arises in WSe$_2$ SPEs due to the intervalley crystal symmetry breaking in the presence of the defects. The zero-phonon line of SPEs in WSe$_2$ typically exhibits a doublet with energy splitting of about 0.7 meV, as shown in Figs. 5(a) and 5(b). The emitters characterized here exhibit slow timescale spectral diffusion similar to that observed in Fig. 2. To clearly illustrate how the SAWs couple to the fine-structure doublets, we correct for the slow spectral diffusion via postprocessing in Fig. 5. SAWs are driven at the 299.4-MHz resonance and three PL spectra are acquired and averaged for each applied SAW drive power. For each averaged spectrum, the peaks are fit to the center frequency and this frequency is subtracted from the spectra taken for the adjacent SAW drive powers. The doublet is thought to arise from asymmetry in the confining potential, which hybridizes the spin and valley states. This hybridization leads to splitting of the SPE transition into orthogonal linearly polarized transitions shown as H and V [41,47,54]. Similar fine-structure splitting effects have been observed in other SPE platforms, most notably III-V QDs [58–60]. In some cases, such as the deterministic generation of linearly polarized photons, fine-structure splitting can be advantageous [61,62], while in others, such as generation of entangled photon pairs via the biexciton-exciton radiative cascade, the fine-structure splitting can be detrimental by reducing the entanglement fidelity [63,64].

Despite observations of the radiative biexciton-exciton cascade in monolayer WSe$_2$ observed here and in prior works [41,65], the nonzero fine-structure splitting has prevented any measurements of polarization entanglement with 2D materials.

SAW control of the single-photon emission is a unique, on-chip mechanism to manipulate the fine-structure splitting features. As shown in Figs. 5(a) and 5(b), the excitonic peak with its associated polarization can be split into two peaks with an energy spacing tuned by the applied SAW IDT power. In a specific range of powers, the H and V transitions overlap, resulting in a steady-state PL spectrum consisting of three Lorentzians for which the side peaks are vertically and horizontally polarized and the central peak becomes a mixture of the two polarizations. By aligning an optical bandpass filter to the central peak, the collected photons are reminiscent of an atomiclike emitter without fine structure, and the SAW modulation may serve as a mechanism to erase the fine structure altogether, although at a cost of reduced brightness. The SAW-mediated fine-structure mixing may find immediate applications for entangled-photon-pair generation from WSe$_2$ SPEs through the radiative biexciton cascade, whereby the emission of a photon from the biexciton-to-exciton transition leads to a second photon emitted from the exciton-to-ground state transition [inset to Fig. 5(a)]. Indeed, for many SPEs, we observe exciton-biexciton transitions with fine-structure split doublets, as shown in the top panel of Fig. 5(c). When turning on the SAW drive power at 299.4 MHz, the deformation potential mixes the transitions in the central regions highlighted in the bottom panel of Fig. 5(c).

VI. DISCUSSION

The underlying mechanism of the fine-structure mixing still remains an interesting open question worth future investigation. Two potential mechanisms can be envisioned to cause the mixing and are illustrated in Fig. 6. First, similar to Fig. 1(a), due to oscillating compressive and tensile strain, the band gap of WSe$_2$ oscillates at the SAW frequency, causing the atomic level transitions to renormalize and oscillate as well. In this picture (type-I mechanism), the atomistic description of the two-level system that is responsible for the fine-structure splitting remains relatively the same, and the two fine-structure peaks oscillate in phase with one another. This mechanism would only appear to have their fine-structure splitting removed on the central peak due to the slow timescale of the steady-state PL measurements. For the second possible mechanism (type-II mechanism), the single-particle wavefunctions of the ground and excited states become compressed and elongated across the strain axis, which also causes the fine-structure transition energies to oscillate. Here, however, the fundamental mechanism of the
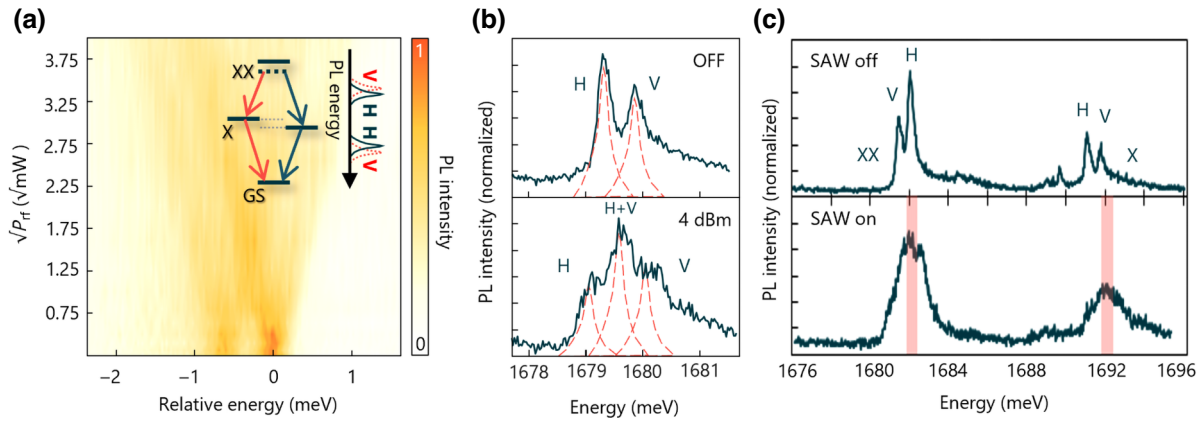
FIG. 5. Deformation potential coupling and fine-structure mixing of the exciton-biexciton radiative cascade in monolayer WSe$_2$. (a) Contour map showing the increase in ΔE with applied IDT power to a SAW cavity mode at 299.4 MHz. The data have been corrected for slow spectral diffusion to assist in visualizing the SAW coupling to the fine-structure-split states. The emission energy is scaled relative to the highest-energy ZPL state for this emitter. Inset demonstrates a conceptual illustration of biexciton-exciton radiative cascade from WSe$_2$ emitters with nonzero fine-structure splitting. GS, X, and XX denote the ground-state, exciton, and biexciton states. (b) Fine-structure splitting of a representative single-photon emitter in WSe$_2$ with horizontally (H) and vertically (V) polarized transitions split into a doublet separated by 0.7 meV. Bottom panel demonstrates mixing of the single-photon emitter's fine-structure states when injecting phonons into the SAW mode at 299.4 MHz. The characteristic double-peak spectrum of SAW-modulated SPEs is observed for both the H and V transitions, which results in a single threefold Lorentzian in which the central peak arises from mixing of the H and V transitions. (c) Mixing of the emission from fine-structure states of the exciton-biexciton-like cascade in WSe$_2$ upon SAW modulation. The top panel shows the emission spectrum for no applied SAW power with the characteristic set of doublets corresponding to the excitonlike (X) and biexcitonlike (XX) transitions. The bottom panel shows the spectrum from the same emitter with SAW modulation. The doublets merge as demonstrated in (b), and the highlighted region demonstrates the energies at which the fine-structure splitting is erased by mixing both the H and V photons.

oscillation is not band-gap renormalization, but instead strain-induced modification to the atomic morphology of the defect. In this case, similar to control of the fine-structure splitting via strain in III-V QDs [66], the compressive and tensile strain can restore the system symmetry associated with the exchange interaction, eliminating the fine structure altogether. In the case of the type-I mechanism, the central Lorentzian appearing in the PL spectra would become a mixed state of H and V polarized light on slow timescales relative to the inverse of the fine-structure splitting. In the case of the type-II mechanism, the central Lorentzian is a coherent entangled state. These two scenarios, on a slow timescale of steady-state PL, lead to the same spectral response, and given that their polarimetric density matrices are identical, they cannot be distinguished from each other with polarization state tomography. It is plausible that both mechanisms, each acting with different strengths depending on the orientation of the SAW propagation and emitter's dipole axis, are simultaneously occurring. These observations also unveil additional possibilities; for example, examining whether rearranging the order of successive photons in the type-I case (when the oscillation is in phase) could lead to the creation of an entangled state is worth exploring. Additionally, the frequency modulation of the doublets allows for simultaneous temporal and spectral filtering that can mitigate dephasing

and restore indistinguishability, albeit at the expense of optical brightness [67].

To compare the potential of single-photon emitters in 2D materials for optomechanical applications, a holistic approach is required. As evidenced by our experiments, WSe$_2$ emitters show a higher sensitivity to deformation potential coupling than h-BN. This is expected given that the ratio of the photon energy to the band gap for WSe$_2$ is considerably lower than that for h-BN. Hence, to first order, the transition in WSe$_2$ is more sensitive to small modulations of the band gap. Additionally, WSe$_2$ emitters are hypothesized to arise from an interplay between the defects and strain, where a valley-symmetry-breaking defect located at a strained region comes into resonance with the dark exciton energy in WSe$_2$ and becomes a viable pathway for the radiative recombination of the dark exciton as single-photon light [41,47]. Given the crucial role of strain in the microscopic origin of WSe$_2$ emitters, we also expected a higher deformation potential coupling. This has in fact also been observed in other studies, where, on average, higher deformation potential coupling for WSe$_2$ emitters has been measured compared to h-BN; however, to our knowledge, this is the first work that compares the deformation potential coupling on the same platform, and using the same methods, which allows us to further corroborate this conclusion [52,68,69]. Lastly, SPEs in WSe$_2$
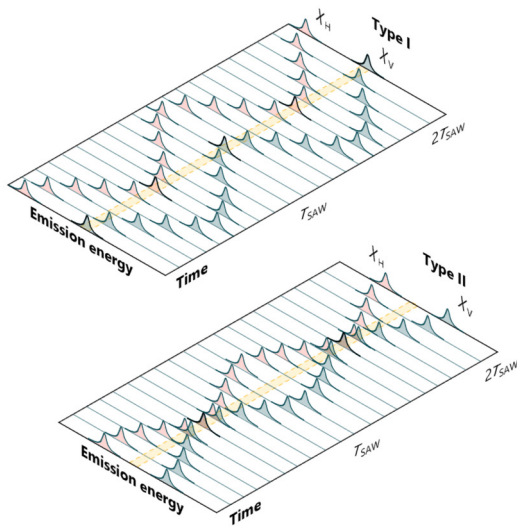
FIG. 6. Prospective mechanisms for fine-structure mixing of the exciton-biexciton radiative cascade in monolayer WSe_2. Schematic illustration of two possible mechanisms for the observed fine-structure mixing. Here X_H and X_V denote the "H"- and "V"-polarized exciton FSS transitions, respectively. In the experiments, spectral filtering is indicated by the yellow shaded region, which highlights the optical energy bandwidth of detected photons. For the type-I mechanism, the two fine-structure peaks oscillate in phase with one another with a period T_{SAW} corresponding to the inverse of the SAW modulation frequency. As a result, photons emitted at the X_H and X_V energies exhibit a time delay for when they overlap with the spectral filter. For the type-II mechanism, the peaks oscillate at the SAW frequency out of phase, resulting in synchronization and elimination of the fine-structure splitting altogether due to the strain induced by the SAW.

are known to exist in the monolayer and bilayer forms of WSe_2, whereas in *h*-BN, high-quality SPEs appear in multilayer forms of *h*-BN. Given the overall low *c*-axis thermal conductivity in 2D materials, it is expected that strain transfer to monolayer or bilayer materials would exceed that of multilayer flakes and allow us to observe higher deformation potential coupling in monolayer WSe_2; however, larger deformation potential coupling only translates to larger vacuum optomechanical coupling g_0, and for optomechanical applications, factors such as brightness, purity, linewidth, and indistinguishability are also crucial factors that require attention in order to engineer coherent quantum mechanical systems using 2D material hosts. The purity and brightness of *h*-BN and WSe_2 SPEs are relatively on par with each other; however, as also apparent from our results, *h*-BN SPEs demonstrate higher stability and lower-frequency jitter. In *h*-BN, while the deformation potential coupling is weaker than in WSe_2 by a factor of 4, Fourier-limited SPE emission from *h*-BN red emitters have been observed with linewidths as low as 25 MHz [36] and the generation of indistinguishable photons [35], whereas the smallest linewidth observed in WSe_2 emitters to our

knowledge is 2.5 GHz [70]. This implies that reaching a sideband-resolved regime and coherent photon-phonon interactions in *h*-BN may be more feasible in the near future using higher-frequency SAW cavities and resonant excitation schemes. In addition to this, reports of possible spin ground states in *h*-BN would, in our opinion, make *h*-BN SPEs a more suitable platform for quantum optomechanics that include photons, phonons, and spins. While the current iteration of the SPE-SAW resonator is in the initial stage of development with the resonator operating in a fully classical regime, the next generation of devices requires reducing the mode volume and increasing the operation frequency to the gigahertz range to reach the sideband-resolved regime. This would allow for coherent quantum phenomena to be observed, such optical sideband pumping to herald the generation of single-cavity phonons [21], photon-phonon entangled states, and acoustically driven Rabi oscillations [17].

VII. CONCLUSION

In summary, acoustic control of single-photon emitters in monolayer WSe_2 and multilayer *h*-BN integrated with $LiNbO_3$ surface acoustic wave resonators is demonstrated through electromechanical and optomechanical spectroscopy. The observed single-photon emitter modulation is consistent with deformation potential coupling through strain with sensitivity of at least 35 meV/% for WSe_2, and 12.5 meV/% for *h*-BN. We demonstrate a near-term application of classical control of 2D material emitters through SAW-mediated single-photon frequency modulation and high-speed fine-structure manipulation, which may open the door for demonstrations of entangled-photon-pair generation from 2D materials. The integration of 2D materials with gigahertz-frequency SAW resonators in the future would enable operation in the quantum regime with demonstrations of sideband-resolved excitation and detection, quantum transduction, and photon-phonon entanglement.

The data that support the findings in this study are available from the corresponding author upon reasonable request.
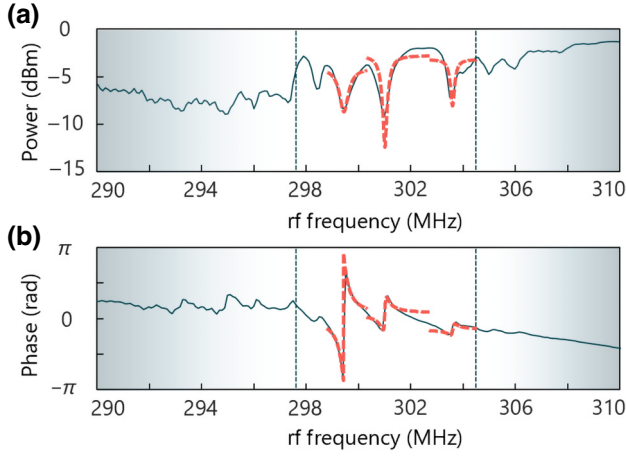
FIG. 7. Extended data: resonance quality factor fits. (a) Cavity reflection spectrum magnitude, $|S_{11}|$, showing modes centered around 300 MHz. Vertical dashed lines and gradient areas represent the Bragg mirror band edges. Fits to each $|S_{11}|$ mode are denoted by dashed red lines. (b) Corresponding phase data for the cavity reflection spectrum are shown. The corresponding phase fits to each $|S_{11}|$ mode fit are denoted by dashed red lines.

and S.D.P. performed steady-state PL spectroscopy, time-resolved PL spectroscopy, second-order autocorrelation, stroboscopic PL measurements, and S-parameter measurements. All authors discussed the results and commented on the manuscript at all stages.

The authors declare no conflicts of interest.

APPENDIX A: ELECTROMECHANICAL CHARACTERIZATION

The S_{11} scattering parameter was measured to ascertain the intrinsic quality factor, Q_i, and external quality factor, Q_e, of the SAW resonator. The output from a vector network analyzer (VNA) was sent to the single port of the SAW resonator IDT. The reflected signal from the resonator was sent back to the VNA, and the magnitude and phase of S_{11} were measured as a function of rf frequency at 4.4 K. Figures 7(a) and 7(b) show representative results from this measurement. Dips in the $|S_{11}|$ spectrum within the bandwidth of the SAW resonator mirrors (about 298–304 MHz) are indicative of the different SAW resonator modes. By simultaneously fitting the magnitude and phase at each resonance frequency to

$$S_{11}(f) = \frac{(Q_{e,n} - Q_{i,n})/Q_{e,n} + 2iQ_{i,n}(f - f_n)/f}{(Q_{e,n} + Q_{i,n})/Q_{e,n} + 2iQ_{i,n}(f - f_n)/f}, \quad (A1)$$

we extract both Q_i and Q_e for each resonance. Table I summarizes the results from the fits for each of the cavity resonances measured after transferring the 2D flakes.

TABLE I. Intrinsic (Q_i) and external (Q_e) quality factors for each of the SAW resonator modes.

	f_{SAW} (MHz)			
	298.425	299.425	300.975	303.561
Q_i	1300	3000	1600	1700
Q_e	5900	800	2300	6000

APPENDIX B: DEVICE FABRICATION

SAW resonators were fabricated on bulk 128° YX-cut lithium niobate, which is a piezoelectric substrate with high electromechanical coupling ($K^2 = 5.4\%$). A representative optical image of the SAW resonators is shown in Fig. 8(a).

As shown in the fabrication flow diagram in Fig. 8(b), the resonators were fabricated with 20 nm of NbN deposited by dc magnetron reactive sputtering. Distributed Bragg grating mirrors were then patterned using optical lithography and inductively coupled plasma reactive ion etching with CF_4 chemistry. Various cavity lengths L were fabricated, where $L = d + 2L_m$. The inner SAW mirror edges are separated by d and the modes penetrate the mirrors by $L_m = w/r_s \approx 130$ μm for a NbN width $w = 10$ μm and single-period reflectivity $r_s \approx 0.02$ [71]. One-port SAW resonators were fabricated by placing a NbN IDT within the SAW resonator. Contact pads composed of 10 nm of Ti and 90 nm of Au were deposited using a lift-off process. Finally, monolayer WSe_2 flakes were identified using mechanical exfoliation and high-contrast optical imaging. Monolayers were then integrated within the SAW resonator using an all-dry transfer method. An optical image of the cavity after transfer is shown in Fig. 8(a). After the device fabrication was completed, the samples were attached to an Oxygen-free high-conductivity copper mount that holds both the sample and printed circuit board (PCB), and the devices were wire-bonded prior to the experiments.

APPENDIX C: ACOUSTO-OPTICAL MICROSCOPY

A 532-nm continuous-wave laser source was used for the steady-state and stroboscopic measurements. A dichroic mirror at 540 nm was used to separate the optical excitation and collection paths. An additional 600 nm long-pass optical filter was used to further extinguish the excitation laser in the collection path. An infinity-corrected 0.55-NA objective with 13-mm working distance was used for spectroscopy. Samples were placed on a customized radio-frequency (rf) PCB sample carrier for microwave connection and were cooled to 4.4 K inside a Montana S200 cryostation. Optical spectra were acquired using a Princeton instruments HRS-500 with 300/1200/1800 groove/mm gratings and a thermoelectrically cooled Pixis
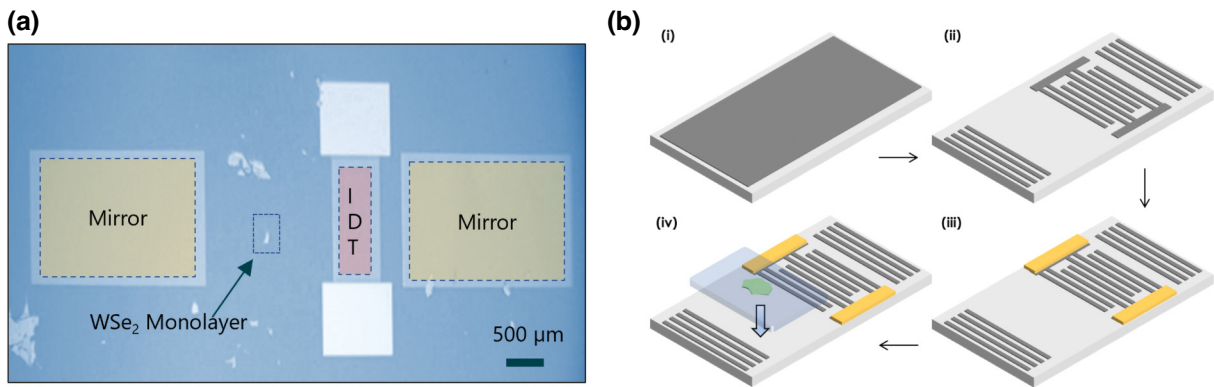
FIG. 8.   Extended data: fabrication process flow for the WSe$_2$-SAW devices. (a) An optical image of the completed device is shown. The WSe$_2$ monolayer is indicated by the dashed line box. The IDT and mirrors are respectively highlighted in red and yellow dashed boxes. (b) The process flow for fabricating the devices includes (i) NbN sputter deposition, (ii) optical lithography and a dry etch process, (iii) Ti/Au metal deposition and liftoff for wire-bond pads, and (iv) 2D material transfer using an all-dry viscoelastic technique.

silicon CCD. Second-order autocorrelation measurements with continuous-wave optical excitation were performed by utilizing the spectrometer as a monochromator to filter the emission from individual emitters. The optical signals were then collected in a multimode fiber beam splitter connected to two single-photon avalanche detectors (Excelitas SCPM-AQRH-13-FC). Swabian time-tagging electronics were used for photon counting. A schematic of the steady-state PL spectroscopy is illustrated in Fig. 9(a).

Time-resolved photoluminescence measurements were performed using a 660-nm, 80-MHz repetition rate pulsed laser source and single-photon counting. For stroboscopic measurements, the internal oscillator of the rf signal generator for driving the SAW IDT was connected to an external clock generator for synchronization between the SAW and detected photons. The external clock provided a pulsed signal with $f_{rf}/30$ to the start channel of the photon-counting module. The emitter photoluminescence detected after the monochromator with the single-photon detector was connected to the stop channel, and a histogram of start-stop times was constructed as the spectrometer grating was scanned across the modulated SPE resonances. A schematic of the time-resolved PL spectroscopy is illustrated in Fig. 9(b).
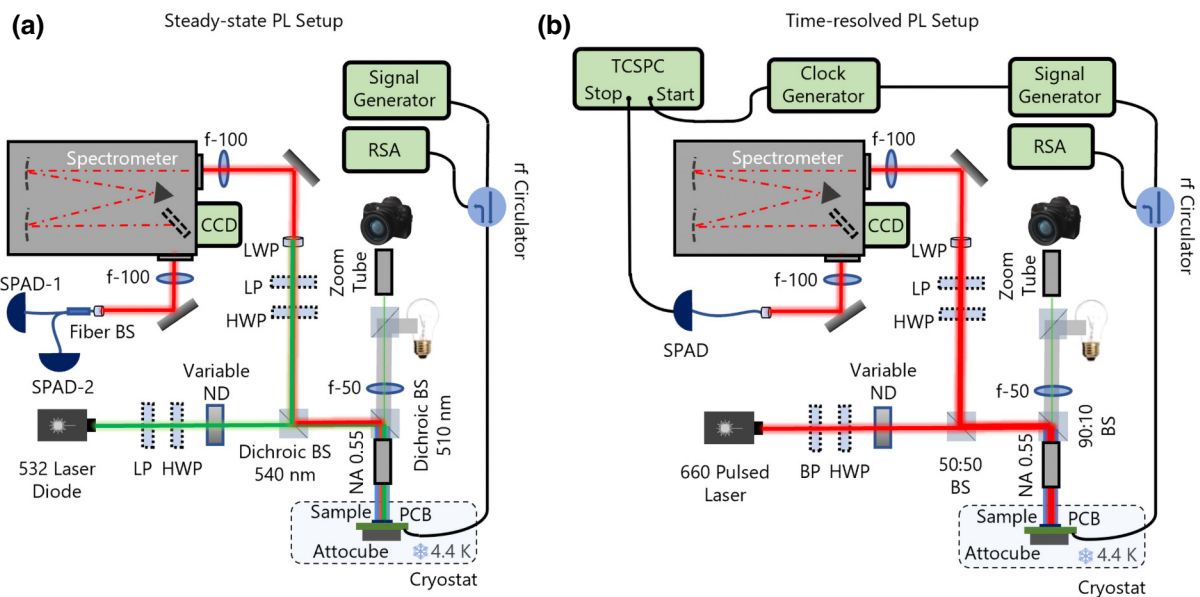

FIG. 9.   Extended data: photoluminescence (PL) spectroscopy setup. (a) The steady-state PL setup is shown. Components illustrate capability for imaging on the charge-coupled device (CCD) and second-order autocorrelation measurements. (b) The PL setup for time-resolved spectroscopy, mainly the stroboscopic measurement, is illustrated.
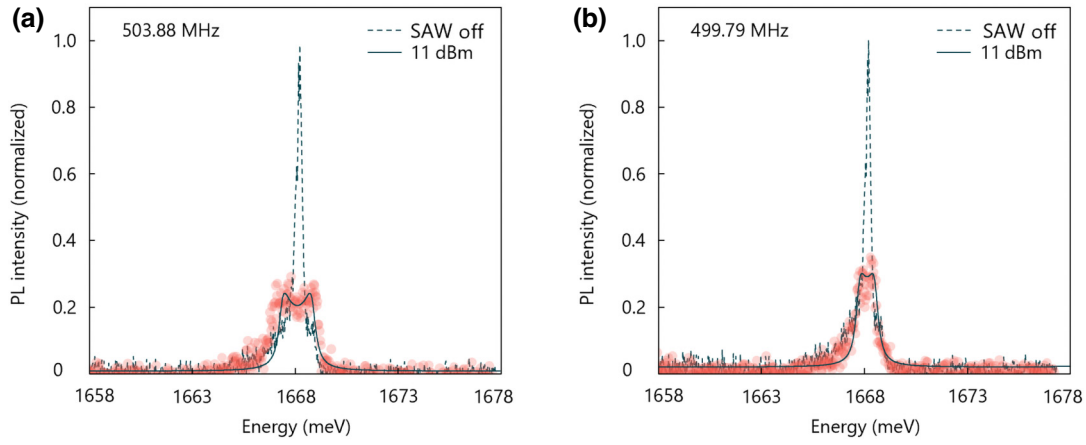
FIG. 10.   Extended data: spectral fits to a Lorentzian lineshape with a temporal sinusoidal oscillation SAW modulation of a SPE is shown. A SPE from an additional sample, a resonant cavity centered at 500 MHz, is shown. (a) SPE emission under no applied SAW power is indicated via a dashed line. An applied power of 11 dBm at a resonant cavity mode of 503.88 MHz results in a dual-peak spectrum whose fit is shown via a solid line. We extract $\Delta E = 0.62$ meV from the fit. (b) Power applied to the same SPE at a different resonant cavity mode, 499.79 MHz, exhibiting $\Delta E = 0.285$ meV splitting extracted from a fit to a temporally oscillating Lorentzian function.

APPENDIX D: FITTING OF THE ZPL SPLIT-PEAK STRUCTURE

The observed double-peak structure of the ZPL under SAW modulation is indicative of SAW-SPE coupling. The PL signals are fit to a Lorentzian function modulated by a sinusoidal interaction in the time domain given by

$$I(E) = I_0 + f_{\mathrm{rf}} \frac{2A}{\pi} \int_0^{1/f_{\mathrm{rf}}} \frac{\omega}{4(E - (E_0 + \xi))^2 + \omega^2} \, dt, \tag{D1}$$
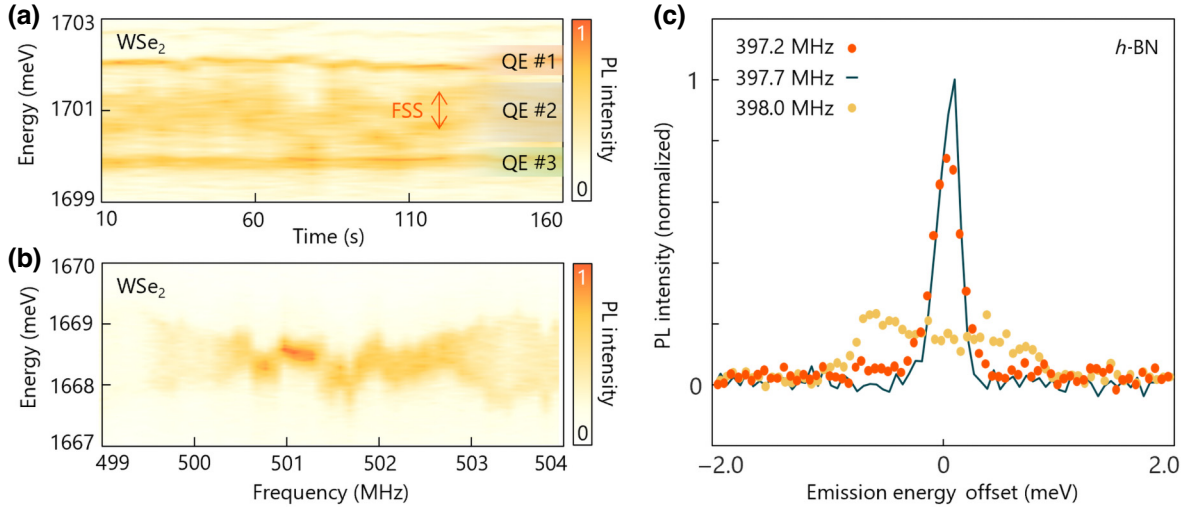

FIG. 11.   Extended data: WSe$_2$ emitter stability and spectral jitter stability of WSe$_2$ emitters are reported. (a) Time evolution of WSe$_2$ emitters is shown, where separate quantum emitters are denoted by QE. Emitter 2 exhibits fine-structure splitting as indicated by an arrow. Both peaks corresponding to emitter 2 exhibit correlated spectral jitter on a timescale of tens of seconds. (b) Frequency-dependent energy modulation of a WSe$_2$ emitter on a SAW cavity centered around 500 MHz is presented. The emitter exhibits charge noise-induced spectral jitter comparable to that shown in Fig. 2(a). (c) Line spectra at select frequencies from Fig. 2(c) are shown. The spectrum at cavity mode 398.0 MHz exhibits stronger SAW-emitter coupling compared to the 397.2-MHz cavity mode. The off-resonant spectrum at 397.7 MHz indicates that both cavity modes at 397.2 and 398.0 MHz couple to the emitter at differing extents.
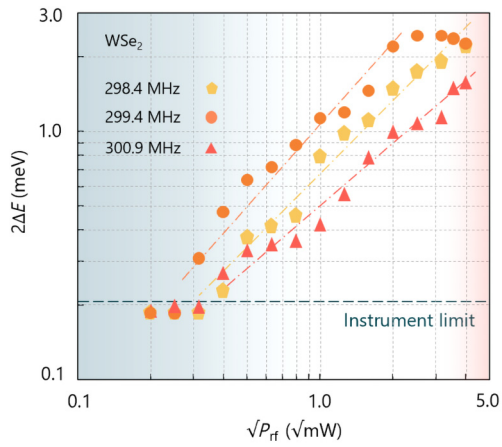
FIG. 12. Extended data: power dependence of a WSe$_2$ emitter lineshape splitting demonstrating deformation potential coupling ΔE is shown as a function of applied power to the SAW IDT. Data for a WSe$_2$ emitter coupled to resonant SAW cavity modes at 298.4, 299.4, and 300.9 are shown. Fits to the power-dependent splitting for the WSe$_2$ emitters yield slopes of 1.045, 0.976, and 0.841 meV/$\sqrt{\text{mW}}$ for modes at 298.4, 299.4, and 300.9 MHz, respectively, indicating deformation potential coupling.

where I_0 is an offset, A is the amplitude, E_0 is the center energy, ω is the width of the Lorentzian emission peak, ξ is $\Delta E \sin(2\pi f_{\text{rf}} t)$, and ΔE is the optomechanical modulation amplitude of the SPE, which can be extracted. PL signals shown in Figs. 1(c), 1(e), and 10 show data fitted to Eq. (D1). The ΔE versus P_{rf} scaling shown in Fig. 4 is obtained similarly.

APPENDIX E: TIME-DOMAIN SAW SIMULATIONS

To understand and predict the temporal dynamics of the stroboscopic measurements, we carried out temporal simulations in MATLAB®. In the classical regime, the spectral response of the system at any given time can be denoted as

$$\Omega(t) = \frac{\Gamma}{1 + (\omega - \omega_\circ - \Delta E \sin(2\pi f_{\text{rf}}))^2/\Gamma^2}, \quad \text{(E1)}$$

where Γ and $\omega_\circ$ are the radiative decay rate and the frequency of the emitter and ΔE and f_{rf} are the amplitude of the SAW modulation and frequency of the SAW. The monochromator is modeled as a square pulse in frequency space as $U(\omega_l) - U(\omega_h)$, where ω_l and ω_h are the low-pass and high-pass corner frequencies of an ideal bandpass filter. While performing the stroboscopic measurement, the counts on the single-photon detector would follow $\Omega(t)(U(\omega_l) - U(\omega_h))$. The fit to the data is calculated using this expression for an emitter with a lifetime of 2 ns, a nonradiatively broadened linewidth of 2 meV, and an ideal bandpass filter with a bandwidth of 3 meV, where

the filter is set on the high-energy wing of the spectral response.

APPENDIX F: FINITE-ELEMENT SIMULATIONS OF SAW CAVITY

A COMSOL Multiphysics® finite-element simulation was used to model the strain amplitude at the location of the WSe$_2$ emitter. A two-dimensional simulation was constructed representing a cross section of the LiNbO$_3$-NbN SAW cavity along the propagation direction and the surface normal. Material parameters for LiNbO$_3$ were extracted from Ref. [72], and the elastic, piezoelectric, and permittivity tensors were then rotated 38° to simulate a 128° YX-cut LiNbO$_3$ substrate. NbN reflectors and IDT electrodes were simulated with electrostatic floating-potential and terminal and ground boundary conditions, respectively. The coupled piezoelectric equations of motion were solved using a frequency-domain simulation with 0-dBm power applied to the IDT electrodes. Perfectly matched layers were applied to the boundaries of the simulation domain to absorb any scattered radiation. The strain amplitude was extracted by taking the maximum value of the tensile strain component oriented along the SAW propagation direction between the IDT and the NbN reflector placed further from the IDT. Over the frequency range of 299–301 MHz, a maximum tensile strain amplitude of 0.0119% at 0-dBm applied IDT power coincided with a SAW cavity resonance at 299.665 MHz, in good agreement with the observed resonance at 299.425 MHz from the S_{11} parameter measurement.

---

[1] P. Delsing, *et al.*, The 2019 surface acoustic waves roadmap, J. Phys. D: Appl. Phys. **52**, 353001 (2019).

[2] M. J. A. Schuetz, E. M. Kessler, G. Giedke, L. M. K. Vandersypen, M. D. Lukin, and J. I. Cirac, Universal quantum transducers based on surface acoustic waves, Phys. Rev. X **5**, 031031 (2015).

[3] A. H. Safavi-Naeini, D. Van Thourhout, R. Baets, and R. Van Laer, Controlling phonons and photons at the wavelength scale: Integrated photonics meets integrated phononics, Optica **6**, 213 (2019).

[4] A. Jayich, J. Sankey, B. Zwickl, C. Yang, J. Thompson, S. Girvin, A. Clerk, F. Marquardt, and J. Harris, Dispersive optomechanics: A membrane inside a cavity, New J. Phys. **10**, 095008 (2008).

[5] R. W. Andrews, R. W. Peterson, T. P. Purdy, K. Cicak, R. W. Simmonds, C. A. Regal, and K. W. Lehnert, Bidirectional and efficient conversion between microwave and optical light, Nat. Phys. **10**, 321 (2014).

[6] J. T. Hill, A. H. Safavi-Naeini, J. Chan, and O. Painter, Coherent optical wavelength conversion via cavity optomechanics, Nat. Commun. **3**, 1196 (2012).

[7] K. C. Balram, M. I. Davanço, J. D. Song, and K. Srinivasan, Coherent coupling between radiofrequency, optical

and acoustic waves in piezo-optomechanical circuits, Nat. Photonics **10**, 346 (2016).

[8] M. J. Burek, N. P. De Leon, B. J. Shields, B. J. Hausmann, Y. Chu, Q. Quan, A. S. Zibrov, H. Park, M. D. Lukin, and M. Loncar, Free-standing mechanical and photonic nanostructures in single-crystal diamond, Nano Lett. **12**, 6084 (2012).

[9] B. A. Moores, L. R. Sletten, J. J. Viennot, and K. W. Lehnert, Cavity quantum acoustic device in the multimode strong coupling regime, Phys. Rev. Lett. **120**, 227701 (2018).

[10] L. R. Sletten, B. A. Moores, J. J. Viennot, and K. W. Lehnert, Resolving phonon Fock states in a multimode cavity with a double-slit qubit, Phys. Rev. X **9**, 021056 (2019).

[11] M. M. de Lima and P. V. Santos, Modulation of photonic structures by surface acoustic waves, Rep. Prog. Phys. **68**, 1639 (2005).

[12] R. A. DeCrescent, Z. Wang, P. Imany, R. C. Boutelle, C. A. McDonald, T. Autry, J. D. Teufel, S. W. Nam, R. P. Mirin, and K. L. Silverman, Large single-phonon optomechanical coupling between quantum dots and tightly confined surface acoustic waves in the quantum regime, Phys. Rev. Appl. **18**, 034067 (2022).

[13] M. Choquer, M. Weiß, E. D. Nysten, M. Lienhart, P. Machnikowski, D. Wigger, H. J. Krenner, and G. Moody, Quantum control of optically active artificial atoms with surface acoustic waves, IEEE Trans. Quantum Eng. **3**, 5100217 (2022).

[14] D. A. Golter, T. Oo, M. Amezcua, K. A. Stewart, and H. Wang, Optomechanical quantum control of a nitrogen-vacancy center in diamond, Phys. Rev. Lett. **116**, 143602 (2016).

[15] D. A. Golter, T. Oo, M. Amezcua, I. Lekavicius, K. A. Stewart, and H. Wang, Coupling a surface acoustic wave to an electron spin in diamond via a dark state, Phys. Rev. X **6**, 041060 (2016).

[16] M. J. Burek, J. D. Cohen, S. M. Meenehan, N. El-Sawah, C. Chia, T. Ruelle, S. Meesala, J. Rochman, H. A. Atikian, M. Markham, et al., Diamond optomechanical crystals, Optica **3**, 1404 (2016).

[17] S. J. Whiteley, G. Wolfowicz, C. P. Anderson, A. Bourassa, H. Ma, M. Ye, G. Koolstra, K. J. Satzinger, M. V. Holt, F. J. Heremans, A. N. Cleland, D. I. Schuster, G. Galli, and D. D. Awschalom, Spin–phonon interactions in silicon carbide addressed by Gaussian acoustics, Nat. Phys. **15**, 490 (2019).

[18] J. R. Gell, M. B. Ward, R. J. Young, R. M. Stevenson, P. Atkinson, D. Anderson, G. A. C. Jones, D. A. Ritchie, and A. J. Shields, Modulation of single quantum dot energy levels by a surface-acoustic-wave, Appl. Phys. Lett. **93**, 81115 (2008).

[19] M. Metcalfe, S. M. Carr, A. Muller, G. S. Solomon, and J. Lawall, Resolved sideband emission of InAs/GaAs quantum dots strained by surface acoustic waves, Phys. Rev. Lett. **105**, 37401 (2010).

[20] E. D. Nysten, A. Rastelli, and H. J. Krenner, A hybrid (Al)GaAs-LiNbO$_3$ surface acoustic wave resonator for cavity quantum dot optomechanics, Appl. Phys. Lett. **117**, 121106 (2020).

[21] P. Imany, Z. Wang, R. A. DeCrescent, R. C. Boutelle, C. A. McDonald, T. Autry, S. Berweger, P. Kabos, S. W. Nam, R.

P. Mirin, et al., Quantum phase modulation with acoustic cavities and quantum dots, Optica **9**, 501 (2022).

[22] M. Lienhart, M. Choquer, E. D. Nysten, M. Weiß, K. Müller, J. J. Finley, G. Moody, and H. J. Krenner, Heterogeneous integration of superconducting thin films and epitaxial semiconductor heterostructures with lithium niobate, J. Phys. D: Appl. Phys. **56**, 365105 (2023).

[23] S. I. Azzam, K. Parto, and G. Moody, Prospects and challenges of quantum emitters in 2D materials, Appl. Phys. Lett. **118**, 240502 (2021).

[24] M. Kianinia, Z.-Q. Xu, M. Toth, and I. Aharonovich, Quantum emitters in 2D materials: Emitter engineering, photophysics, and integration in photonic nanostructures, Appl. Phys. Rev. **9**, 011306 (2022).

[25] A. Srivastava, M. Sidler, A. V. Allain, D. S. Lembke, A. Kis, and A. Imamoğlu, Optically active quantum dots in monolayer WSe$_2$, Nat. Nanotechnol. **10**, 491 (2015).

[26] Y.-M. He, G. Clark, J. R. Schaibley, Y. He, M.-C. Chen, Y.-J. Wei, X. Ding, Q. Zhang, W. Yao, X. Xu, C.-Y. Lu, and J.-W. Pan, Single quantum emitters in monolayer semiconductors, Nat. Nanotechnol. **10**, 497 (2015).

[27] C. Chakraborty, L. Kinnischtzke, K. M. Goodfellow, R. Beams, and A. N. Vamivakas, Voltage-controlled quantum light from an atomically thin semiconductor, Nat. Nanotechnol. **10**, 507 (2015).

[28] M. Koperski, K. Nogajewski, A. Arora, V. Cherkez, P. Mallet, J. Y. Veuillen, J. Marcus, P. Kossacki, and M. Potemski, Single photon emitters in exfoliated WSe$_2$ structures, Nat. Nanotechnol. **10**, 503 (2015).

[29] P. Tonndorf, R. Schmidt, R. Schneider, J. Kern, M. Buscema, G. A. Steele, A. Castellanos-Gomez, H. S. van der Zant, S. M. de Vasconcellos, and R. Bratschitsch, Single-photon emission from localized excitons in an atomically thin semiconductor, Optica **2**, 347 (2015).

[30] T. T. Tran, C. Elbadawi, D. Totonjian, C. J. Lobo, G. Grosso, H. Moon, D. R. Englund, M. J. Ford, I. Aharonovich, and M. Toth, Robust multicolor single photon emission from point defects in hexagonal boron nitride, ACS Nano **10**, 7331 (2016).

[31] N. R. Jungwirth, B. Calderon, Y. Ji, M. G. Spencer, M. E. Flatté, and G. D. Fuchs, Temperature dependence of wavelength selectable zero-phonon emission from single defects in hexagonal boron nitride, Nano. Lett. **16**, 6052 (2016).

[32] G. Grosso, H. Moon, B. Lienhard, S. Ali, D. K. Efetov, M. M. Furchi, P. Jarillo-Herrero, M. J. Ford, I. Aharonovich, and D. Englund, Tunable and high-purity room temperature single-photon emission from atomic defects in hexagonal boron nitride, Nat. Commun. **8**, 705 (2017).

[33] Y. Luo, G. D. Shepard, J. V. Ardelean, D. A. Rhodes, B. Kim, K. Barmak, J. C. Hone, and S. Strauf, Deterministic coupling of site-controlled quantum emitters in monolayer WSe$_2$ to plasmonic nanocavities, Nat. Nanotechnol. **13**, 1137 (2018).

[34] H. Zhao, M. T. Pettes, Y. Zheng, and H. Htoon, Site-controlled telecom-wavelength single-photon emitters in atomically-thin MoTe$_2$, Nat. Commun. **12**, 6753 (2021).

[35] C. Fournier, S. Roux, K. Watanabe, T. Taniguchi, S. Buil, J. Barjon, J.-P. Hermier, and A. Delteil, Two-photon interference from a quantum emitter in hexagonal boron nitride, Phys. Rev. Appl. **19**, L041003 (2023).

[36] A. Dietrich, M. Doherty, I. Aharonovich, and A. Kubanek, Solid-state single photon source with Fourier transform limited lines at room temperature, Phys. Rev. B **101**, 081401 (2020).

[37] J. R. Schaibley, H. Yu, G. Clark, P. Rivera, J. S. Ross, K. L. Seyler, W. Yao, and X. Xu, Valleytronics in 2D materials, Nat. Rev. Mater. **1**, 1 (2016).

[38] A. L. Exarhos, D. A. Hopper, R. N. Patel, M. W. Doherty, and L. C. Bassett, Magnetic-field-dependent quantum emission in hexagonal boron nitride at room temperature, Nat. Commun. **10**, 1 (2019).

[39] H. L. Stern, Q. Gu, J. Jarman, S. Eizagirre Barker, N. Mendelson, D. Chugh, S. Schott, H. H. Tan, H. Sirringhaus, I. Aharonovich, *et al.*, Room-temperature optically detected magnetic resonance of single defects in hexagonal boron nitride, Nat. Commun. **13**, 1 (2022).

[40] Y. Luo, N. Liu, X. Li, J. C. Hone, and S. Strauf, Single photon emission in WSe$_2$ up 160 K by quantum yield control, 2D Mater. **6**, 035017 (2019).

[41] K. Parto, S. I. Azzam, K. Banerjee, and G. Moody, Defect and strain engineering of monolayer WSe$_2$ enables site-controlled single-photon emission up to 150 K, Nat. Commun. **12**, 3585 (2021).

[42] A. Branny, S. Kumar, R. Proux, and B. D. Gerardot, Deterministic strain-induced arrays of quantum emitters in a two-dimensional semiconductor, Nat. Commun. **8**, 15053 (2017).

[43] C. Palacios-Berraquero, D. M. Kara, A. R.-P. Montblanch, M. Barbone, P. Latawiec, D. Yoon, A. K. Ott, M. Loncar, A. C. Ferrari, and M. Atatüre, Large-scale quantum-emitter arrays in atomically thin semiconductors, Nat. Commun. **8**, 15093 (2017).

[44] C. Fournier, A. Plaud, S. Roux, A. Pierret, M. Rosticher, K. Watanabe, T. Taniguchi, S. Buil, X. Quélin, J. Barjon, J. Barjon, J.-P. Hermier, and A. Delteil, Position-controlled quantum emitters with reproducible emission wavelength in hexagonal boron nitride, Nat. Commun. **12**, 3779 (2021).

[45] K. Parto, S. I. Azzam, N. Lewis, S. D. Patel, S. Umezawa, K. Watanabe, T. Taniguchi, and G. Moody, Cavity-enhanced 2D material quantum emitters deterministically integrated with silicon nitride microresonators, Nano Lett. **22**, 9748–9756 (2022).

[46] S. Lazić, A. Espinha, S. Pinilla Yanguas, C. Gibaja, F. Zamora, P. Ares, M. Chhowalla, W. S. Paz, J. J. Burgos, A. Hernández-Mínguez, P. V. Santos, and H. P. van der Meulen, Dynamically tuned non-classical light emission from atomic defects in hexagonal boron nitride, Commun. Phys. **2**, 113 (2019).

[47] L. Linhart, M. Paur, V. Smejkal, J. Burgdörfer, T. Mueller, and F. Libisch, Localized intervalley defect excitons as single-photon emitters in WSe$_2$, Phys. Rev. Lett. **123**, 146401 (2019).

[48] A. Castellanos-Gomez, M. Buscema, R. Molenaar, V. Singh, L. Janssen, H. S. Van Der Zant, and G. A. Steele, Deterministic transfer of two-dimensional materials by all-dry viscoelastic stamping, 2D Mater. **1**, 011002 (2014).

[49] R. Manenti, M. J. Peterer, A. Nersisyan, E. B. Magnusson, A. Patterson, and P. J. Leek, Surface acoustic wave resonators in the quantum regime, Phys. Rev. B **93**, 041411 (2016).

[50] E. D. S. Nysten, A. Rastelli, and H. J. Krenner, A hybrid (Al)GaAs-LiNbO$_3$ surface acoustic wave resonator for cavity quantum dot optomechanics, Appl. Phys. Lett. **117**, 121106 (2020).

[51] M. Koperski, K. Nogajewski, A. Arora, V. Cherkez, P. Mallet, J.-Y. Veuillen, J. Marcus, P. Kossacki, and M. Potemski, Single photon emitters in exfoliated WSe$_2$ structures, Nat. Nanotechnol. **10**, 503 (2015).

[52] S. Kumar, A. Kaczmarczyk, and B. D. Gerardot, Strain-induced spatial and spectral isolation of quantum emitters in mono- and bilayer WSe$_2$, Nano Lett. **15**, 7567 (2015). pMID: 26480237.

[53] J. Dang, S. Sun, X. Xie, Y. Yu, K. Peng, C. Qian, S. Wu, F. Song, J. Yang, S. Xiao, *et al.*, Identifying defect-related quantum emitters in monolayer WSe$_2$, npj 2D Mater. Appl. **4**, 1 (2020).

[54] C. Chakraborty, N. R. Jungwirth, G. D. Fuchs, and A. N. Vamivakas, Electrical manipulation of the fine-structure splitting of WSe$_2$ quantum emitters, Phys. Rev. B **99**, 045308 (2019).

[55] P. Jiang, X. Qian, and R. Yang, Time-domain thermoreflectance (TDTR) measurements of anisotropic thermal conductivity using a variable spot size approach, Rev. Sci. Instrum. **88**, 074901 (2017).

[56] J. Pustiowski, K. Müller, M. Bichler, G. Koblmüller, J. J. Finley, A. Wixforth, and H. J. Krenner, Independent dynamic acousto-mechanical and electrostatic control of individual quantum dots in a LiNbO$_3$-GaAs hybrid, Appl. Phys. Lett. **106**, 013107 (2015).

[57] N. Mendelson, M. Doherty, M. Toth, I. Aharonovich, and T. T. Tran, Strain-induced modification of the optical characteristics of quantum emitters in hexagonal boron nitride, Adv. Mater. **32**, 1908316 (2020).

[58] M. Bayer, G. Ortner, O. Stern, A. Kuther, A. Gorbunov, A. Forchel, P. Hawrylak, S. Fafard, K. Hinzer, T. Reinecke, *et al.*, Fine structure of neutral and charged excitons in self-assembled in In(Ga)As/(Al)GaAs quantum dots, Phys. Rev. B **65**, 195315 (2002).

[59] R. Seguin, A. Schliwa, S. Rodt, K. Pötschke, U. Pohl, and D. Bimberg, Size-dependent fine-structure splitting in self-organized InAs/GaAs quantum dots, Phys. Rev. Lett. **95**, 257402 (2005).

[60] C. F. Schuck, R. Boutelle, K. Silverman, G. Moody, and P. J. Simmonds, Single-photon generation from self-assembled GaAs/InAlAs(111)A quantum dots with ultrasmall fine-structure splitting, J. Phys.: Photonics **3**, 024012 (2021).

[61] H. Wang, Y.-M. He, T.-H. Chung, H. Hu, Y. Yu, S. Chen, X. Ding, M.-C. Chen, J. Qin, X. Yang, *et al.*, Towards optimal single-photon sources from polarized microcavities, Nat. Photonics **13**, 770 (2019).

[62] S. Gerhardt, M. Deppisch, S. Betzold, T. H. Harder, T. C. Liew, A. Predojević, S. Höfling, and C. Schneider, Polarization-dependent light-matter coupling and highly indistinguishable resonant fluorescence photons from quantum dot-micropillar cavities with elliptical cross section, Phys. Rev. B **100**, 115305 (2019).

[63] A. Hudson, R. Stevenson, A. Bennett, R. Young, C. Nicoll, P. Atkinson, K. Cooper, D. Ritchie, and A. Shields, Coherence of an entangled exciton-photon state, Phys. Rev. Lett. **99**, 266802 (2007).

[64] R. M. Stevenson, R. J. Young, P. Atkinson, K. Cooper, D. A. Ritchie, and A. J. Shields, A semiconductor source of triggered entangled photon pairs, Nature **439**, 179 (2006).

[65] Y.-M. He, O. Iff, N. Lundt, V. Baumann, M. Davanco, K. Srinivasan, S. Höfling, and C. Schneider, Cascaded emission of single photons from the biexciton in monolayered WSe$_2$, Nat. Commun. **7**, 13409 (2016).

[66] S. Seidl, M. Kroner, A. Högele, K. Karrai, R. J. Warburton, A. Badolato, and P. M. Petroff, Effect of uniaxial stress on excitons in a self-assembled quantum dot, Appl. Phys. Lett. **88**, 203113 (2006).

[67] A. Bennett, R. Patel, A. Shields, K. Cooper, P. Atkinson, C. Nicoll, and D. Ritchie, Indistinguishable photons from a diode, Appl. Phys. Lett. **92**, 193503 (2008).

[68] C. Chakraborty, A. Mukherjee, H. Moon, K. Konthasinghe, L. Qiu, W. Hou, T. Peña, C. Watson, S. M. Wu, D. Englund, *et al.*, Strain tuning of the emission axis of quantum emitters in an atomically thin semiconductor, Optica **7**, 580 (2020).

[69] O. Iff, D. Tedeschi, J. Martín-Sánchez, M. Moczała-Dusanowska, S. Tongay, K. Yumigeta, J. Taboada-Gutiérrez, M. Savaresi, A. Rastelli, P. Alonso-González, *et al.*, Strain-tunable single photon sources in WSe$_2$ monolayers, Nano Lett. **19**, 6931 (2019).

[70] S. Kumar, M. Brotóns-Gisbert, R. Al-Khuzheyri, A. Branny, G. Ballesteros-Garcia, J. F. Sánchez-Royo, and B. D. Gerardot, Resonant laser spectroscopy of localized excitons in monolayer WSe$_2$, Optica **3**, 882 (2016).

[71] D. Morgan, *Surface Acoustic Wave Filters with Applications to Electronic Communications and Signal Processing* (Elsevier Science, 2007), ISBN 9780123725370.

[72] R. Tarumi, T. Matsuhisa, and Y. Shibutani, Low temperature elastic constants and piezoelectric coefficients of LiNbO$_3$ and LiTaO$_3$: Resonant ultrasound spectroscopy measurement and lattice dynamics analysis, Jpn. J. Appl. Phys. **51**, 07GA02 (2012).